JOURNAL OF BIOMEDICAL OPTICS 4(1), 28–34 (JANUARY 1999)

SPATIAL DISTRIBUTION OF PHOSPHATE SPECIES IN MATURE AND NEWLY GENERATED MAMMALIAN BONE BY HYPERSPECTRAL RAMAN IMAGING

Jerilyn A. Timlin,[†] Angela Carden,[†] Michael D. Morris,[†] Jeffrey F. Bonadio,[‡] C. Edward Hoffler II,[*] Kenneth M. Kozloff,[*,] and Steven A. Goldstein[*,**]**

[†]University of Michigan, Department of Chemistry, Ann Arbor, Michigan 48109; [‡]University of Michigan Medical School, Department of Pathology, Ann Arbor, Michigan 48109; [*]University of Michigan Medical School, Orthopaedic Research Laboratories, Orthopaedic Surgery, Ann Arbor, Michigan 48109; [**]University of Michigan, Department of Biomedical Engineering, Ann Arbor, Michigan 48109

(Paper BVS-03 received July 8, 1998; accepted for publication Sep. 30, 1998.)

ABSTRACT

Hyperspectral Raman images of mineral components of trabecular and cortical bone at 3 μm spatial resolution are presented. Contrast is generated from Raman spectra acquired over the 600–1400 cm^{-1} Raman shift range. Factor analysis on the ensemble of Raman spectra is used to generate descriptors of mineral components. In trabecular bone independent phosphate (PO_4^{-3}) and monohydrogen phosphate (HPO_4^{-2}) factors are observed. Phosphate and monohydrogen phosphate gradients extend from trabecular packets into the interior of a rod. The gradients are sharply defined in newly regenerated bone. There, HPO_4^{-2} content maximizes near a trabecular packet and decreases to a minimum value over as little as a 20 μm distance. Incomplete mineralization is clearly visible. In cortical bone, factor analysis yields only a single mineral factor containing both PO_4^{-3} and HPO_4^{-2} signatures and this implies uniform distribution of these ions in the region imaged. Uniform PO_4^{-3} and HPO_4^{-2} distribution is verified by spectral band integration. © *1999 Society of Photo-Optical Instrumentation Engineers.* [S1083-3668(99)00301-9]

Keywords Raman imaging; cortical bone; trabecular bone; microscopy.

1 INTRODUCTION

Bone formation is not a single process, but a collection of distinct pathways to synthesize calcified tissues.[1] In developing embryos, the process includes the proliferation and commitment of mesenchymal cells to the skeletal lineage; the patterning of anlage, which is associated with progenitor cell proliferation, migration, and differentiation; and the growth and remodeling of skeletal tissues into a mature form. In postnatal organisms, the bone formation process involves both physiological growth and remodeling and pathological repair and regeneration (i.e., following injury).

Bone is well understood as a composite material that consists of a hydrated, collagen-rich extracellular matrix and carbonated calcium phosphate.[1] However, the fundamental chemical mechanisms dictating the formation of an organized composite are unknown. A clearer understanding of the chemistry of bone formation can lead to improved prevention and therapy for congenital deformities and metabolic disorders as well as for fracture management.

The thermodynamically most stable mineral in bone is a nonstoichiometric calcium phosphate arranged in an apatitic lattice, although there may be other mineral phases present in the earliest stages of mineralization.[2] In fully mineralized lamellar bone, the calcium phosphate lattice contains substantial amounts of carbonate and small, but readily observable, amounts of monohydrogen phosphate. Smaller amounts of fluoride, chloride and other ions may also be present. As bone advances from the initial stages of formation to full maturity, the degree of lattice substitution and mineralization varies. In less mineralized bone there is a larger relative amount of monohydrogen phosphate and a smaller relative amount of carbonate.[3,4]

Bone macroscopic structure may be classified as cortical or trabecular. Cortical bone is dense, compact bone primarily located in the diaphysis or cen-

Address all correspondence to Michael D. Morris, Department of Chemistry, 930 North University Ave., Ann Arbor, MI 48109-1055. Tel: (734) 764-7360; Fax: (734) 764-8815; E-mail: mdmorris@umich.edu

tral length of long bones. Cortical bone is continuously renewed through a process called remodeling. Tissue is resorbed and then replaced in a temporally and spatially coupled process. The process that mediates cortical remodeling begins with osteoclasts tunneling through the tissue mass creating their own vascular supply and following a trajectory nearly parallel to the shaft of the diaphysis. The tissue newly synthesized by the osteoblasts forms an osteon, a tubular structure with concentric lamellae. Mineralization within an osteon occurs at a changing rate with the first 60% of the mineral being deposited very rapidly and the remainder very slowly.[5] Different sectors of the cortical diaphysis are remodeled at different rates, likely due to regional variations in mechanical demands.[6] Within a sector bone turnover is relatively uniform, leading to subtle mineral gradients within the tissue.

Trabecular bone, or spongy bone, consists of plates and rods that create a lattice-like structure. This structure provides a large effective surface area resulting in enhanced load distribution and energy absorption. Trabecular bone is located at the ends of long bones in the metaphysis and in vertebrae. Like cortical bone, remodeling in trabecular bone is also accomplished through resorption coupled to formation, but the resulting microstructure is different from that of osteons. Bone at the surface of a rod or plate is replaced by a longitudinal bundle of tissue called a trabecular packet. Lamellae are oriented along the length of the packet. Calcium homeostasis causes remodeling in trabecular tissue to occur more frequently than in cortical tissue, and the newly deposited packets located at the surfaces of trabeculae are much less calcified than the more central tissue, leading to sharp mineral gradients across trabecular plates and rods.[7]

Vibrational spectroscopy has a long history in bone and tooth chemistry. Most work has been performed in the infrared, because protein fluorescence has hindered Raman spectroscopy with the green lasers that dominated practice until the mid-1980s. Typically, bone Raman spectra have been obtained on deproteinated specimens. Although it is possible that the deproteination process generates artifacts, this approach has allowed the acquisition of mineral spectra of mature and newly formed bone with green laser excitation.[8] In recent years, the use of near-infrared lasers has solved the protein fluorescence problem. Fourier transform (FT)-Raman spectroscopy has been used to obtain mineral and protein Raman spectra from bone.[9,10]

In the wake of recent technological advances, vibrational spectroscopic imaging is becoming increasingly popular for the analysis of complex organized systems, such as bones and teeth. For example, de Grauw et al. have used Raman microscopy to achieve 0.5 μm spatial resolution at 512 points along a line at the interface between crystalline calcium phosphate and a section of bone.[11] Dental adhesive diffusion into dentin has been imaged using Raman microspectroscopy.[12] Marcott et al. have reported 4096 pixel (33 μm$\times$33 μm pixels) infrared spectroscopic images of canine alveolar bone tissue.[13] They showed matrix and mineral images, as well as a mineral maturity image. We have reported hyperspectral Raman images of mature and newly regenerated canine trabecular bone with 20 000 pixel (1.4 μm$\times$1.4 μm pixel) definition.[14] The images clearly showed the lowest phosphate (PO_4^{-3}) content in the newly modeled bone. They also demonstrated that there is a severe spectral overlap between the methacrylate mounting media and phosphate ν_1 (958 cm^{-1}).

Multivariate data reduction has been widely used in magnetic resonance imaging[15] and fluorescence imaging.[16] Our group has employed factor analysis to extract information from sets of 500–2000 solution Raman spectra.[17] We have applied the same technique to Raman imaging to generate chemical composition contrast in bone[14] and in aluminosilicate glasses[18] and crystallinity contrast in syndiotactic polystyrene.[19]

2 EXPERIMENTAL DATA

All bone samples were obtained from the Orthopaedic Research Laboratories at the University of Michigan. In the current study both canine trabecular and human cortical bone were imaged.

2.1 TRABECULAR BONE SPECIMENS

A specimen was obtained from canine tibia in which osteotomy surgery was performed and new bone was allowed to spontaneously regenerate within the osteotomy gap. The gap tissue was excised, fixed in 70% ethanol, embedded in a polymethylmethacrylate (PMMA) resin using standard protocols, and sectioned into 40$\times$15$\times$0.02 mm slices. Because bone formation occurs from the surgical margin inward, this specimen contained new bone with a maturity/mineralization gradient, i.e., with the least mature bone nearest the center of the osteotomy gap. Slices were mounted on a standard glass microscope slide, as shown in Figure 1, so that the gradient of bone formation was along the long dimension of the slide.

The bone specimen was imaged at two locations along the mineralization gradient. Area A was mature bone that was a distance from the defect wall and area B was in the bone formation region, i.e., the trabecular bone in its earliest phases of mineralization.

2.2 CORTICAL BONE SPECIMENS

For comparison to trabecular bone, a fresh, unfixed transverse section of human cortical bone was imaged. The specimen was an anterior femur diaphysis of a 41-year-old male obtained from the Univer-

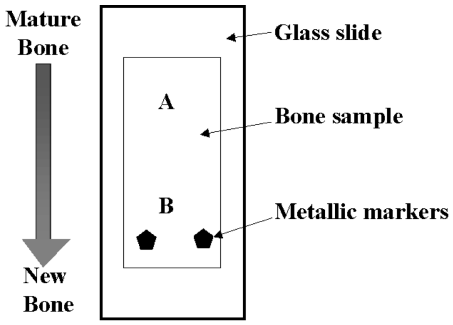

Fig. 1 Schematic of a mounted canine trabecular bone specimen. This is a longitudinal cross section of a cylindrical defect showing the bone mineralization gradient along the long axis.

sity of Michigan Anatomical Donations Program. Because of the difficulty of micromachining thin sections of unmounted bone, a large specimen block, 2 cm×1 cm×1 cm, was cut with a diamond saw. The specimen was surface polished with progressive grades of silicon carbide paper and finished with a 0.25 μm diamond slurry. The specimen was stored frozen and imaged in a nitrogen atmosphere to minimize the growth of aerobic bacteria.

2.3 HYPERSPECTRAL LINE IMAGING SYSTEM

The hyperspectral line imaging system was described previously in the literature.[18–20] In the current application, a 250 mW 785 nm laser (SDL, Inc.) was used as the excitation source. A 5×/0.25 numerical aperture (NA) Fluar objective (Zeiss) was used to illuminate the specimen and it collected backscattered Raman-shifted light. At this magnification the height of a charge coupled device (CCD) pixel corresponds to 1.4 μm at the specimen. To generate square pixels, the microscope stage was incremented 1.4 μm/frame. The spectral resolution was 8 cm^{-1}. Typically, either 100 or 200 spectral/spatial frames were acquired to yield 100×100 pixel images (140 μm×140 μm) or 100×200 pixel images (140 μm×280 μm). The anaerobic chamber for imaging unfixed bone was constructed by encasing the microscope stage in a flexible plastic chamber and blowing a stream of house nitrogen through it.

All data analysis was performed in MATLAB (Mathworks, Inc.) using vendor-supplied and locally written scripts. Before applying any multivariate techniques the cosmic events (spikes) were filtered out of the data and the data were corrected for curvature resulting from spectrograph geometry.

Details of the factor analysis procedure are given elsewhere.[18] In brief, the covariance matrix of the corrected data set was calculated and it was used to generate the principal components (eigenvectors). Factors were constructed from the first few principal components and were chosen to account for 99.99+% of the total signal generated. The number of components to be retained was determined by inspection of the scree plots of the eigenvalues and confirmed by inspection of the score images of the first few eigenvectors. Although the eigenvectors retained give a mathematical representation of the chemical species in the data, they are linear combinations of the underlying Raman spectra and the eigenvectors must be rotated to have physical meaning, i.e., in order to represent Raman spectra. The factor rotation was guided by non-negativity and by second-derivative constraints that are known to be valid for Raman spectra.

Table 1 Raman band assignments for bone.

Vibration	Canine trabecular bone (cm^{-1})	Human osteonal bone (cm^{-1})	Band position[a] (cm^{-1})
PO_4^{-3}, ν_4	598	583	583
PO_4^{-3}, ν_1	958	958	960
HPO_4^{-2}, ν_3	1000	1003	1003
PO_4^{-3}, ν_3	1032	1031	1028–1055
CO_3^{-2}, ν_1	1065	1070	1070
Amide III	1243	1244	1245
CO_3^{-2}, C=O stretch	1274 (weak)	1270	1270
C-H bending	1450	1447	1450
Amide I	Not observed	1660	1660

[a] From Refs. 9 and 10.

3 SPECTROSCOPIC CONSIDERATIONS

Table 1 lists mineral and matrix Raman bands of trabecular and cortical bone identified in this study as well as in previous work.[10,21] Representative spectra from the specimens are shown in Figure 2.

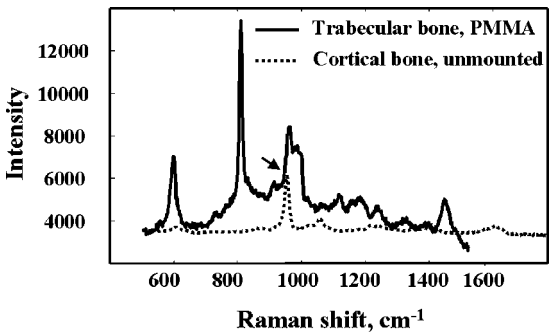

Fig. 2 Representative Raman spectra of PMMA-mounted canine trabecular bone and fresh human cortical bone. The small arrow indicates the phosphate ν_1 band, which is a shoulder on the stronger PMMA band.

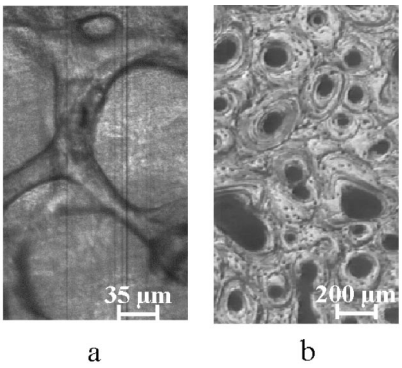

Fig. 3 (a) Bright-field transmission image of canine trabecular bone, 200 μm×400 μm. (b) Bright-field reflectance image of human cortical bone 800 μm×1400 μm.

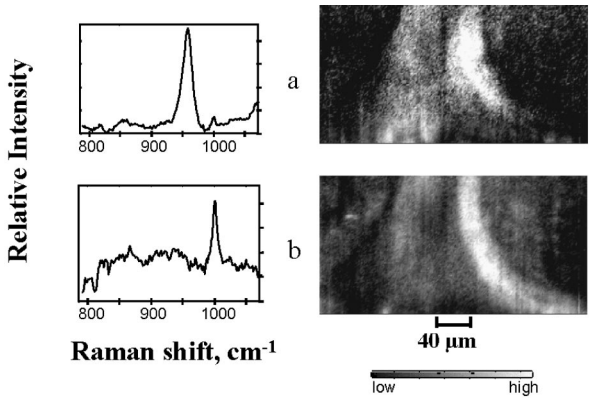

Fig. 4 Factors and score images of a 275 μm×140 μm region of mature canine trabecular bone strut. (a) PO_4^{-3}; (b) HPO_4^{-2}. The score image contrast was adjusted for clarity.

In mature bone, the principal spectroscopic markers are the PO_4^{-3} asymmetric stretch (ν_3, ~1030 cm^{-1}) and the PO_4^{-3} symmetric stretch (ν_1, ~960 cm^{-1}).[22] Because the mineral lattice is heavily substituted with carbonate, the carbonate bands at 1070 and 1270 cm^{-1} are readily identified. In newly formed bone and in matrix vesicles spectral bands characteristic of monohydrogen phosphate (HPO_4^{-2}) are seen. Collagen bands are also observed.

Figure 2 shows spectra from both specimens. The solid spectrum clearly demonstrates the spectral interference of the mounting media, PMMA, and of PO_4^{-3} ν_1. An arrow points to the PO_4^{-3} band that appears as a shoulder on a much larger PMMA band. The most common alternative mounting media, epoxy based resins, have a clear window around the phosphate ν_1 stretch, but interfere with the HPO_4^{-2} stretch near 1000 cm^{-1}. In general, the spectrum of any mounting medium is likely to overlap at least some bands in the bone spectrum. Only unfixed unmounted bone completely avoids the spectral interference problem. However, it is necessary to image unmounted bone frozen or in an anaerobic chamber to prevent bacterial growth.

4 RAMAN IMAGES OF MATURE AND NEWLY FORMED TRABECULAR BONE

Figure 3 contains light microscope images of the two bone specimens. Small regions of these specimens were chosen for Raman imaging. The appearance of both specimens is normal.

Figure 4 shows two factors and their corresponding score (Raman factor contrast) images from mature trabecular bone. A total of six factors is needed to describe the data set. Two of these are the Raman background and residual fluorescence, probably from iron. Another two are PMMA Raman scatter.[14] These factors do not contain information on bone chemistry and are not shown here.

The factor of Figure 4(a) is representative of the Raman signal from PO_4^{-3} and that of Figure 4(b) indicative of the Raman signal from HPO_4^{-2}. The factors represent Raman signatures, but do not contain information as to the intensity on the ordinate axis. Instead, information regarding the intensity is located in the intensities of the score images. In a nonstoichiometric material in which the composition varies from point to point factor analysis does not necessarily yield complete Raman spectra. Instead, the factors correspond to the signatures of spatially varying structural motifs or components such as ions. Similar behavior is observed in aluminosilicate glasses.[18]

The PO_4^{-3} factor is dominated by the 958 cm^{-1} band and the score image maps the location of the most fully mineralized bone strut. The HPO_4^{-2} factor is dominated by the 1000 cm^{-1} band and maps incompletely mineralized bone. This bone specimen is mature bone, but even in mature bone there are sites of remodeling where new bone formation and regeneration occur to some extent.

In trabecular bone, remodeling occurs from the surface, so the most mature bone is located in the interior of the mineralized region. The degree of bone maturity decreases toward the edges of each strut. In addition, the surfaces of the trabeculae have a region of relatively unmineralized bone (osteoid). As a result, these surfaces present an opportunity to observe a phosphate ion gradient. Figure 4(b) shows areas of incompletely mineralized bone. These are clearest at the right edge of the strut.

Previously researchers have concluded there would be no penetration of the PMMA into mature bone.[23] Therefore we would expect the PMMA and phosphate images to be complementary, as we have shown.[14]

The score images shown are all of 275 μm×140 μm areas, with spectral resolution of 8 cm^{-1}. None of the images has been smoothed. We define our spatial resolution to be the length of 2 pixels, or 2.8 μm. Using the Rayleigh criterion at 850 nm, the wavelength of a 1000 cm^{-1} Raman shift, the diffraction-limited spatial resolution for our 5×/0.25 NA objective is approximately 2.1 μm.[24] The

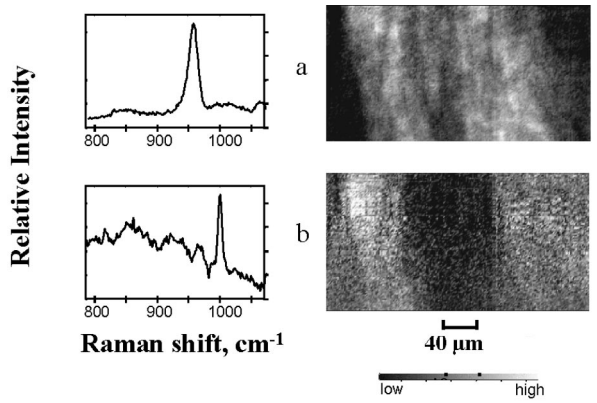

Fig. 5 Factors and score images of a 275 μm×140 μm region of newly modeled canine trabecular bone strut. (a) PO_4^{-3}; (b) HPO_4^{-2}. The score image contrast was adjusted for clarity.

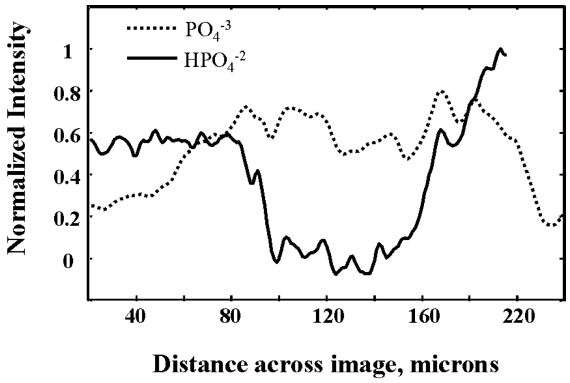

Fig. 6 Phosphate ion distribution across a newly modeled trabecular strut (normalized for total intensity).

measured width of the line projected on the specimen is 2.6±0.2 μm. Although we have not done so here, it is possible to design transfer optics to project a larger image on the spectrograph slit. That change and a 1.3 μm stage increment could be used to generate images with somewhat better spatial resolution. Of course, much better spatial resolution can be achieved by operating with an objective of higher NA. In these experiments we have traded resolution for a larger field of view.

In Figure 5 the PO_4^{-3} and HPO_4^{-2} score images for newly modeled trabecular bone are shown. Again, these images are derived from two of the six factors needed to describe the data. The four background and the PMMA factors are not shown. The field of view and spectral and spatial resolutions are the same as those in the mature bone specimen image of Figure 4.

The PO_4^{-3} score image, Figure 5(a), does reveal some mineralization, but it is discontinuous and the Raman contrast is less intense than it is in mature bone. In fact, to make the contrast visible for reproduction in print, the PO_4^{-3} contrast in Figure 5(a) has been stretched threefold. This adjustment was not necessary for the mature bone PO_4^{-3} score image of Figure 4(a), or for any other image shown in this article. In the newly formed bone small amounts of PMMA can be found penetrating into the mineralized region. Polymer penetration occurs in this case because the bone matrix is not yet completely mineralized. A comparison of Figures 5(a) and 5(b), which contains the HPO_4^{-2} score image, shows that the HPO_4^{-2} is located spatially along the edges of the strut as it is in the mature bone region. In the newly modeled bone, however, the HPO_4^{-2} region is fairly uniform and extends approximately 20 μm into the PO_4^{-3} region. HPO_4^{-2} is also found outside the PO_4^{-3} boundary. This phosphate is probably in trabecular packets.

The Raman contrast along a representative line through the strut is plotted in Figure 6. The plot shows the phosphate species distribution across this newly formed trabecular strut. This plot shows PO_4^{-3} increasing towards the interior of the strut. The steep gradient in HPO_4^{-2} content in the interior is clear. The HPO_4^{-2} signal falls to the background noise level within as little as 20 μm. The formation of PO_4^{-3} is more gradual.

5 RAMAN IMAGES OF AN OSTEONAL REGION OF FRESH CORTICAL BONE

In contrast to the trabecular bone specimen, factor analysis of the cortical bone specimen does not yield separate factors for PO_4^{-3} and HPO_4^{-2}. Instead, a single factor representing mineral content is recovered. This factor contains characteristic frequencies of PO_4^{-3} and HPO_4^{-2}. This factor and the mineral content score image are shown in Figure 7. The 10 000 pixel image is 140 μm×140 μm at 2.8 μm spatial resolution, 8 cm^{-1} spectral resolution. Because only one mineral factor can be isolated, the spatial distribution of the two phosphate ions must be identical to within the resolution limits of our imaging system.

To verify this interpretation of our data, we generated univariate images from the integrated areas

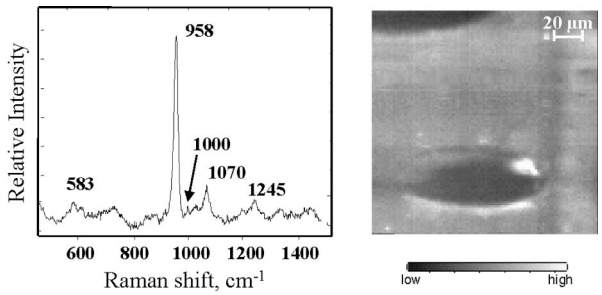

Fig. 7 The mineral content factor and the score image of a 275 μm×140 μm region of human cortical bone.

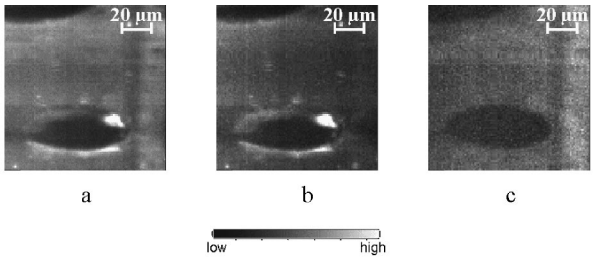

Fig. 8 Univariate band integration images of the cortical bone specimen in Figure 7. (a) PO_4^{-3}; (b) HPO_4^{-2}; (c) ratio image, PO_4^{-3}/HPO_4^{-2}.

under the PO_4^{-3} 958 cm^{-1} band and the HPO_4^{-2} 1003 cm^{-1} band, respectively. These images are shown in Figures 8(a) and 8(b). Figure 8(c) is simply the pixel-by-pixel ratio of Figures 8(a) and 8(b). The ratio image is almost uniform throughout and confirms that the two ions track one another.

The uniformity of phosphate ratios is consistent with locally uniform levels of tissue maturity. Cortical bone is remodeled less frequently than trabecular bone, and this reduces the probability of identifying a region with distinct spatial gradients in phosphate ratios. The region imaged is situated between two closely spaced osteons and it is quite possible that there is no area where the PO_4^{-3}/HPO_4^{-2} ratio changes by an amount that is detectable with our technique. It should be noted that the images in Figure 8 are approximately 10 times the magnification of the bright-field image in Figure 3(b).

In Figures 8(a) and 8(b) there are light areas around the osteon. These may be areas of higher mineral content adjacent to the osteon or they may simply be artifacts of epi-illumination of an irregular surface. This is currently under investigation.

6 CONCLUSIONS

Raman imaging is a powerful tool for the study of bone chemistry. Any chemical or structural information contained in the underlying vibrational spectra can be used for contrast. We have reported only mineral images, but matrix-based images can be generated. Because the spectra are obtained at 800–900 nm, micron spatial resolution is readily achieved and can be exploited to study the boundary region between mineralized tissue and the matrix vesicles from which it is generated. High definition images are easily acquired. The good spatial resolution and the high definition will be useful in future studies of bone formation chemistry.

Acknowledgments

The authors thank Dr. Jeremy Shaver for writing some of the MATLAB scripts. This work was supported in part by the National Institutes of Health through Grant Nos. R01-GM53766 (M.D.M.) and RO1-AR34399 (S.A.G.).

REFERENCES

1. A. Ham, *Histology*, pp. 378–447, Lippincott, Philadelphia (1974).
2. G. Nancollas, M. Lore, L. Perez, C. Richardson, and S. Zawacki, ''Mineral phases of calcium phosphate,'' *Anatom. Record* **224**, 234–241 (1989).
3. C. Rey, V. Renugopalakrishnan, B. Collins, and M. Glimcher, ''Fourier transform infrared spectroscopic study of the carbonate ions in bone mineral during aging,'' *Calcif. Tissue Int.* **49**, 251–258 (1991).
4. C. Rey, M. Shimizu, B. Collins, and M. Glimcher, ''Resolution-enhanced Fourier transform infrared spectroscopy study of the environment of phosphate ions in the early deposits of a solid phase of calcium-phosphate in bone and enamel, and their evolution with age. I: Investigations in the ν_4PO_4 domain,'' *Calcif. Tissue Int.* **46**, 384–394 (1990).
5. A. Parfitt, ''The physiologic and clinical significance of bone histomorphic elata,'' *Bone Histomorphometry Techniques and Interpretation*, R. Recker, Ed., Chemical Rubber Press, Boca Raton, FL (1983).
6. J. Skedros, S. Su, and R. Bloebaum, ''Biomechanical implications of mineral content and microstructural variations in cortical bone of horse, elk, and sheep calcanei,'' *Anatom. Record* **249**, 297–316 (1997).
7. K. Choi, ''Bioengineering,'' p. 106, Thesis, University of Michigan, Ann Arbor, MI (1991).
8. M. A. Walters, Y. C. Leung, N. C. Blumenthal, R. Z. LeGeros, and K. A. Konsker, ''A Raman and infrared spectroscopic investigation of biological hydroxyapatite,'' *J. Inorg. Biochem.* **39**, 193–200 (1990).
9. I. Rehman, R. Smith, L. L. Hench, and W. Bonfield, ''Structural evaluation of human and sheep bone and comparison with synthetic hydroxyapatite by FT-Raman spectroscopy,'' *J. Biomed. Mater. Res.* **29**, 1287–1294 (1995).
10. G. R. Sauer, W. B. Zunic, J. R. Durig, and R. E. Wuthier, ''Fourier transform Raman spectroscopy of synthetic and biological calcium phosphates,'' *Calcif. Tissue Int.* **54**, 414–420 (1994).
11. C. J. de Grauw, C. Otto, and J. Greve, ''Line-scan Raman microspectrometry for biological applications,'' *Appl. Spectrosc.* **51**(11), 1607–1612 (1997).
12. D. M. Wieliczka, M. B. Kruger, and P. Spencer, ''Raman imaging of dental adhesive diffusion,'' *Appl. Spectrosc.* **51**(11), 1593–1596 (1997).
13. C. Marcott, R. C. Reeder, E. P. Paschalis, D. N. Tatakis, A. L. Boskey, and R. Mendolsohn, ''Infrared microscopic imaging of biomineralized tissues using a mercury-cadmium-telluride focal-plane array detector,'' *Cellul. Mol. Biol.* **44**(1), 109–115 (1998).
14. J. A. Pezzuti, M. D. Morris, J. F. Bonadio, and S. A. Goldstein, in Three-Dimensional and Multidimensional Microscopy: Image Acquisition and Processing V; C. J. Cogswell, J.-A. Conchello, J. M. Lerner, T. Lu, and T. Wilson, Eds., *Proc. SPIE* **3261**, 270–276 (1998).
15. P. Geladi and K. Esbensen, ''Regression on multivariate images: Principal component regression for modeling, prediction and visual diagnostic tools,'' *J. Chemom.* **5**, 97–111 (1991).
16. *Fluorescence Imaging Spectroscopy and Microscopy*, X. F. Wang and B. Herman, Eds., Wiley, New York (1996).
17. J. M. Shaver, K. C. Christensen, J. A. Pezzuti, and M. D. Morris, ''Structure of dihydrogen phosphate ion aggregates by Raman-monitored serial dilution,'' *Appl. Spectrosc.* **52**(2), 259–264 (1998).
18. N. L. Jestel and M. D. Morris, ''Hyperspectral Raman line imaging of an aluminosilicate glass,'' *Appl. Spectrosc.* **52**(1), 64–69 (1998).
19. S. L. Zhang, J. A. Pezzuti, M. D. Morris, A. Appadwedula, C. M. Hsiung, and M. A. Leugers, ''Hyperspectral Raman line-imaging of syndiotactic polystyrene crystallinity,'' *Appl. Spectrosc.* **52**(10), 1264–1268 (1998).
20. K. C. Christensen and M. D. Morris, ''Hyperspectral Raman microscopic imaging using Powell lens line illumination,'' *Appl. Spectrosc.* **52**(9), 1145–1147 (1998).

21. R. Smith and I. Rehman, ''Fourier transform Raman spectroscopic studies of human bone,'' *J. Mater. Sci.: Mater. Med.* **5**, 775–778 (1995).
22. S. J. Gadaleta, N. P. Camacho, R. Mendelsohn, and A. L. Boskey, ''Fourier transform infrared microscopy of calcified turkey leg tendon,'' *Calcif. Tissue Int.* **58**, 17–23 (1996).
23. N. L. Pleshko, A. L. Boskey, and R. Mendelsohn, ''An infrared study of the interaction of polymethyl methacrylate with the protein and mineral components in bone,'' *J. Histochem. Cytochem.* **40**(9), 1413–1417 (1992).
24. *Video Microscopy: The Fundamentals*, S. Inoue and K. R. Spring, Eds., Plenum, New York (1997).